CHEMISTRY OF MATERIALS

Article

pubs.acs.org/cm

Sodium Intercalation Mechanism of 3.8 V Class Alluaudite Sodium Iron Sulfate

Gosuke Oyama,[†] Oliver Pecher,[‡] Kent J. Griffith,[‡] Shin-ichi Nishimura,[†,§] Roberta Pigliapochi,[‡] Clare P. Grey,*[,‡] and Atsuo Yamada*[,†,§]

[†]Department of Chemical System Engineering, The University of Tokyo, 7-3-1 Hongo, Bunkyo-ku, Tokyo 113-8656, Japan
[‡]Department of Chemistry, University of Cambridge, Lensfield Road, Cambridge CB2 1EW, United Kingdom
[§]Unit of Element Strategy Initiative for Catalysts & Batteries (ESICB), Kyoto University, Kyoto 615-8510, Japan

Supporting Information

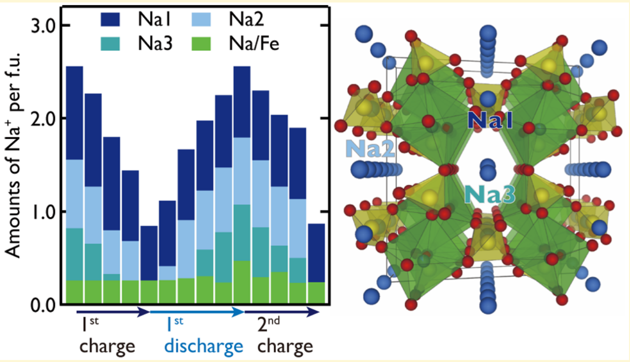

ABSTRACT: Alluaudite sodium iron sulfate $Na_{2+2x}Fe_{2-x}(SO_4)_3$ is one of the most promising candidates for a Na-ion battery cathode material with earth-abundant elements; it exhibits the highest potential among any Fe^{3+}/Fe^{2+} redox reactions (3.8 V vs Na/Na^+), good cycle performance, and high rate capability. However, the reaction mechanism during electrochemical charging/discharging processes is still not understood. Here, we surveyed the intercalation mechanism via synchrotron X-ray diffraction (XRD), ^{23}Na nuclear magnetic resonance (NMR), density functional theory (DFT) calculations, X-ray absorption near edge structure (XANES), and Mössbauer spectroscopy. Throughout charging/discharging processes, the structure undergoes a reversible, single-phase (solid solution) reaction based on a Fe^{3+}/Fe^{2+} redox reaction with a small volume change of ca. 3.5% after an initial structural rearrangement upon the first charging process, where a small amount of Fe irreversibly migrates from the original site to a Na site. Sodium extraction occurs in a sequential manner at various Na sites in the structure at their specific voltage regions.

■ INTRODUCTION

Advanced grid energy storage systems are in great demand to level off-peak and/or intermittent electricity from renewable energy sources (e.g., wind, solar, and tidal). Electrochemical energy storage systems are a promising solution, which can achieve coexistence of high-efficiency, long cycle life, and rapid charge to reduce sudden power spikes without sacrificing cost or safety. As one of the most pragmatic candidates, rechargeable Na-ion batteries have reattracted attention owing to the high natural abundance and even geographical distribution of sodium. To maximize the advantage of Na, positive electrode compounds for Na-ion batteries should consist of Fe or Mn as earth-abundant 3*d* transition metals as redox centers. In this regard, an increasing number of studies have been focused on layered oxides (e.g., O3-type Na_xMO_2,[1,2] P2-type Na_xMO_2,[3] where M = Fe and/or Mn) and phosphates (e.g., olivine-Na_xFePO_4,[4,5] Na_2FePO_4F,[6] $Na_2FeP_2O_7$,[7] $Na_4Fe_3(PO_4)_2(P_2O_7)$[8,9]). Replacing PO_4 units with more electronegative SO_4 units is an effective way to increase the redox potential, which is often referred to as an "inductive effect".[10] Many Li intercalation sulfates generate a high potential (typically 3.5−3.9 V versus Li^+/Li), e.g., tavorite- and triplite-$LiFeSO_4F$,[11,12] KTP-type $KFeSO_4F$,[13] layered $LiFeSO_4OH$,[14] marinite, orthorhombic $Li_2Fe(SO_4)_2$,[15,16] and amarantite-derived $Fe_2O(SO_4)_2$.[17]

Contrary to a step forward of the sulfates in Li systems, Na intercalation compounds reported to date show limited (e.g., $Na_2Fe(SO_4)_2·4H_2O$,[18] kröhnkite $Na_2Fe(SO_4)_2·2H_2O$[19]) or no (e.g., maxwellite-$NaFeSO_4F$,[20] $NaFeSO_4F·2H_2O$[21]) electrochemical activity. Recently, an alluaudite sodium iron sulfate with superior rate capability and the highest potential of 3.8 V (versus Na/Na^+) among any Fe^{3+}/Fe^{2+} redox couples was reported.[22]

The crystal structure of the new compound is essentially isostructural to alluaudite, a common alkaline manganese iron phosphate mineral.[23] As typical for alluaudite compounds, the sodium iron sulfate adopts the monoclinic lattice with *C*2/*c* symmetry with the general formula of $AA'BM_2(XO_4)_3$, where A = Na2, A′ = Na3, B = Na1, M = Fe, and X = S (Figure 1(i)).[23,24] An edge-sharing pair of equivalent FeO_6 octahedra form a Fe_2O_{10} dimer, which is bridged by corner-sharing SO_4 tetrahedra. This unique local Fe coordination results in short Fe−Fe interatomic distances of approximately 3.2 Å, which are likely to contribute to the extremely high redox potential.[24,25] Moreover, inherent deviation from stoichiometry ($x \approx 0.28$ in $Na_{2+2x}Fe_{2-x}(SO_4)_3$, i.e., $Na_{2.56}Fe_{1.72}(SO_4)_3$) and Na replacing Fe on the Fe1 site (referred to Na/Fe1 site) were reported.[24] Thereby, Na occupies

Received: March 16, 2016
Revised: July 4, 2016
Published: July 5, 2016

DOI: 10.1021/acs.chemmater.6b01091
Chem. Mater. 2016, 28, 5321−5328

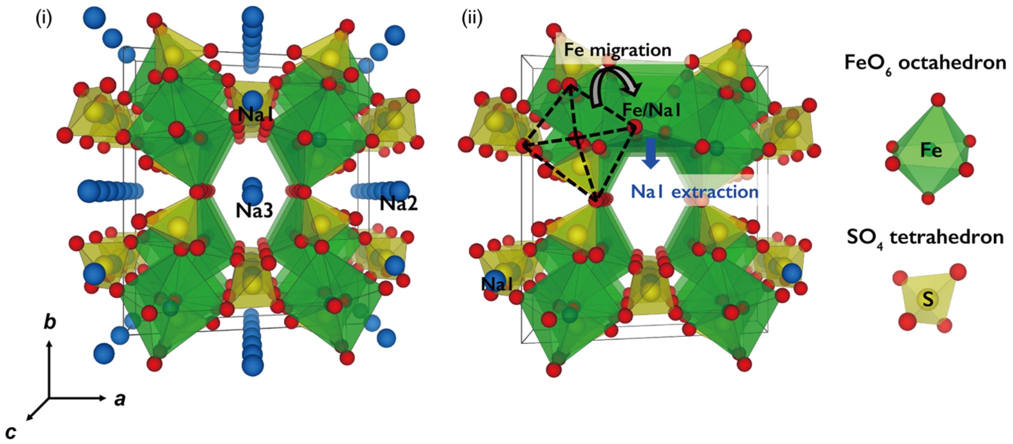

Figure 1. (i) The crystal structure of pristine alluaudite sodium iron sulfate. Sodium and oxygen ions are illustrated in blue and red. Green octahedra and yellow tetrahedra represent FeO_6 and SO_4 units, respectively. Two distinctive Na diffusion channels of Na2 and Na3 are visible along the *c* axis. (ii) The crystal structure of the alluaudite $Na_{2.56-y}Fe_{1.72}(SO_4)_3$ after an irreversible Fe migration from Fe1 to Na1 site upon the first charging process.

four distinctive sites (Na1, Na2, Na3, and Na/Fe1) on Wyckoff positions, 4*e*, 4*b*, 4*e*, and 8*f*, respectively. Two of the four Na sites, Na2 and Na3, are located within one-dimensional open channels as illustrated in Figure 1(i).

To the best of our knowledge, the detailed mechanism of structural changes during electrochemical cycling has not been investigated yet. A clear understanding of electrochemical processes is essential for further performance improvements for this important class of cathode materials. In this work, structural changes during the charging and discharging processes were examined, and the underlying mechanism of the irreversible profile during the first charging process as well as the stabilized behavior in the subsequent cycles were revealed.

■ EXPERIMENTAL SECTION

Synthesis and Electrode Preparation. The alluaudite $Na_{2.56}Fe_{1.72}(SO_4)_3$ powder was synthesized according to the previously reported procedure.[24] All of the galvanostatic charge−discharge measurements for *ex situ* X-ray diffraction (XRD), X-ray absorption near edge (XANES), and Mössbauer spectroscopy measurements were performed with 2032-type coin cells (Hohsen Corp.). Positive electrodes consisted of 80 wt % alluaudite phase, 13 wt % carbon black (Ketjen Black, Lion Corp., ECP), and 7 wt % polytetrafluoro-ethylene (PTFE) binder (provided from an industrial partner). Na metal (Kanto Chemical), glass fiber film (ADVANTEC), and 1 M $NaClO_4$ dissolved in propylene carbonate (PC) (Kishida Chemical) with 2 vol % of fluoroethylene carbonate (FEC)[26] (Kishida Chemical) were used for negative electrodes, separators, and electrolytes, respectively. After the measurements, the cells were disassembled in an Ar filled glovebox (dew point < −70 °C, Miwa Co. Ltd.), and the positive electrode tapes were washed with dimethyl carbonate (DMC) (Kishida Chemical) three times and dried under vacuum to remove impurities. The electrode tapes were packed into Ar filled borosilicate glass tubes (0.3 mm in diameter) for *ex situ* XRD analyses.

Synchrotron XRD. *Ex situ* synchrotron XRD measurements were carried out at KEK PF BL-8B beamline, Tsukuba, Japan. The wavelength was calibrated to be 1.03289 (5) Å. Rietveld refinements and subsequent Fourier difference syntheses were calculated with TOPAS-Academic Ver. 5.0.

Solid-State Nuclear Magnetic Resonance (NMR) Spectroscopy. Solid-state magic angle spinning (MAS) ^{23}Na NMR measurements were conducted on 700, 300, and 200 MHz Bruker Avance I and III spectrometers with respective ^{23}Na Larmor frequencies of 185.2, 79.4, and 52.9 MHz. Hahn-echo pulse sequences with 90° pulse lengths of 1.0 μs were applied. The spectra were acquired with Bruker 1.3 and 2.5 mm MAS probeheads at 60 and 30 kHz spinning frequency, respectively. ^{23}Na shifts were referenced to a 0.1 M NaCl solution in D_2O.[27] All spectra were analyzed using DMFIT.[28] The investigated samples were prepared by chemical oxidation (desodiation) and reduction (sodiation). Chemical oxidation was done using $NOBF_4$ (95%, Aldrich) in acetonitrile under continuous Ar bubbling. The subsequent chemical reduction was conducted using $NaBH_4$ in tetrahydrofuran (THF, Wako Chemical) under Ar atmosphere. After the chemical oxidation/reduction, the powders were washed by pure acetonitrile/THF three times and dried under vacuum at room temperature. The compounds were packed into 1.3 and 2.5 mm ZrO_2 rotors (Bruker) inside an Ar filled glovebox with O_2 and H_2O levels <0.1 ppm to avoid exposure to air and moisture. Oxidation/reduction states of the Fe ions were determined with Mössbauer spectroscopy measurements and resulted in nominal compositions of $Na_{2.56-y}Fe_{1.72}(SO_4)_3$ with $y = 0.0$, 0.41, 0.62, 0.85, and 1.5 for the desodiated samples and $y = 1.0$, 0.67, 0.45, and 0.1 for the sodiated samples (cf. Figure 5(ii)).

X-ray Absorption Near Edge Spectroscopy (XANES). XANES spectra were measured at KEK PF BL-7C. Fe *K*-edge absorption spectra (7080−7180 eV) were collected at room temperature. The X-ray intensity was monitored by ionization chambers in transmission mode using a Si (111) double-crystal monochromator for energy selection. The obtained data were processed with Athena.[29] The electrochemically charged and discharged electrode tapes (about 10 mm in diameter) were applied for the measurements. They were washed with dimethyl carbonate (DMC, Kishida Chemical) and sealed in Ar filled polyethylene films (Asahi Kasei Pax).

Mössbauer Spectroscopy. Mössbauer spectra were measured for electrochemically charged and discharged samples with a Topologic System Inc. spectrometer equipped with a $^{57}Co/Rh$ γ-ray source. The velocity was calibrated by using α-Fe. The electrode tapes were processed in the same way as described for the XANES measurements. The obtained spectra were fitted by Moss Winn (version 3.0) software.

Density Functional Theory (DFT) Calculations. In the calculations, the composition of the pristine $Na_{2.56}Fe_{1.72}(SO_4)_3$ is approximated by $Na_{2.5}Fe_{1.75}(SO_4)_3$. The total energies of $Na_{2.5}Fe_{1.75}(SO_4)_3$ were calculated for various Na-ion geometries. At the minimal energy configuration, the occupancies of Na1, Na2, Na3, and Na/Fe1 sites were 1, 0.75, 0.5, and 0.125, respectively. The Vienna Ab Initio Simulation Package (VASP5.2)[30−32] was implemented within spin-polarized DFT,[33,34] and the projector augmented wave (PAW)[35,36] approach was used to describe the electron−ion core interaction. Full relaxation of the atomic positions and cell parameters and total energy calculations were carried out in the absence of symmetry constraints. The Perdew−Burke−Ernzerhof (PBE)[37,38] exchange-correlation functional was used throughout, applying the Hubbard *U* model[39,40] within the rotationally invariant formalism proposed by Liechstenstein et al.[41] to correct for the known deficiencies of pure functionals for highly localized 3*d* states.[42] A cutoff energy of 520 eV and a 16 *k*-point grid (2 × 2 × 4) were selected for calculations within the four formula unit cell. The threshold difference for self-consistent field (SCF) convergence in the total free energy was set to 1 × 10^{-5} eV. A value of 4.2 eV was chosen for the effective Hubbard interaction parameter $U_{eff} = U - J$ for Fe^{2+} where U is the intraband Coulomb term and J is the intraatomic exchange term.[25,43]

The Fermi contact shifts for the Na sites were calculated from the lowest energy structure. The first-principles solid-state DFT calculations were performed within the CRYSTAL09 linear combinations of atomic orbitals code.[44]

Two hybrid functionals were used, namely, the B3LYP functional [with 20% Hartree−Fock (HF) exchange][45] with a previously shown satisfactory performance for the electronic structure and band gaps of a wide class of materials[45] and for the properties of transition metal compounds[45,46] and a related 35% HF functional[47−49] shown to provide magnetic coupling constants consistent with experimental values.[47,48] Moreover, additional calculations suggest that hybrid functionals with HF exchange in the range from 20% to 35% provide electron−nuclear hyperfine parameters in good agreement with experimental data.[49]

The Fermi contact contribution to the hyperfine shift was computed directly from the spin density at the ^{23}Na nuclear position in the ferromagnetic state and subsequently scaled to a value consistent with the paramagnetic state, as described previously by Kim et al.[50] The Weiss constant and the effective magnetic moment of 12.55 K and 5.20 μ_B, which were obtained by Dwibedi and Barpanda, were applied to evaluate the magnetic parameters defining the temperature dependent paramagnetic susceptibilities of the system.[51]

RESULTS AND DISCUSSION

Electrochemical Charging/Discharging Behavior. Charging/discharging curves and the corresponding differential galvanostatic profiles (dQ/dV) of alluaudite sodium iron sulfate are shown in Figure 2(i). The dQ/dV curve (inset of Figure 2(i)) shows two distinctive redox peaks at 3.67 and 4.06 V upon the first charging process, whereas there are three broad peaks at 3.37, 3.76, and 3.99 V upon the first discharging process as previously reported.[22] Extra capacity exceeding the theoretical capacity was observed on the first charge due to oxidative side reactions of electrolytes and/or carbon additives. Similar changes in the electrochemistry are reported in the case of Li_2FeSiO_4[52,53] and $Li_2FeP_2O_7$,[54,55] where Li−Fe site exchange takes place during the first charging process.

Crystal Structure Changes. To probe the structural changes during electrochemical cycling, *ex situ* XRD measurements and Rietveld refinements were performed for $Na_{2.56-y}Fe_{1.72}(SO_4)_3$ electrodes (Figure 3(i)). Refined lattice parameters a, b, c, and β and the unit cell volume V are given in Figure 3(ii) (refined patterns and refinement indices are shown in Figure S1 and Table S1). For the refinements, the total amounts of Na were fixed to be those calculated by the electrochemical reaction and atomic displacement parameters of the pristine electrode at (a) in Figure 2(i) were used.

Upon the first charging process, the lattice parameters a and c continuously decrease, whereas the lattice parameter b increases after the sharp peak in the dQ/dV plot (d) at 4.06 V. The unit cell volume V shows a gradual shrinkage (ΔV = −2.6% at the fully charged state), consistent with a single-phase (solid-solution) reaction with a small associated volume change, in spite of the extraction of the Na ions, which have a relatively large ionic radius of 1.02 Å.

Upon the first discharging process, the lattice parameters a and c undergo reversible expansion, but b undergoes a partially reversible shrinkage. These changes result in a slightly larger absolute volume change (ΔV = +3.5%) than seen in the first charging process. Upon the second charging process, the lattice parameters and the unit cell volume show reversible change (ΔV = −3.4%). Overall, the irreversible change was only detected in the first charging process, and the reaction was totally reversible in the following cycles, which is consistent with a good cycle performance. The observed small volume change might be due to the three-dimensional open framework of the alluaudite structure and its off-stoichiometric composition.

Even after all the Fe^{2+} ions have been oxidized to Fe^{3+} in the nonstoichiometric $Na_{2.56}Fe_{1.72}(SO_4)_3$, 0.84 mol of Na ions remain in the 3D framework, which may function as binding pillars. Indeed, first principle calculations predict that the volume

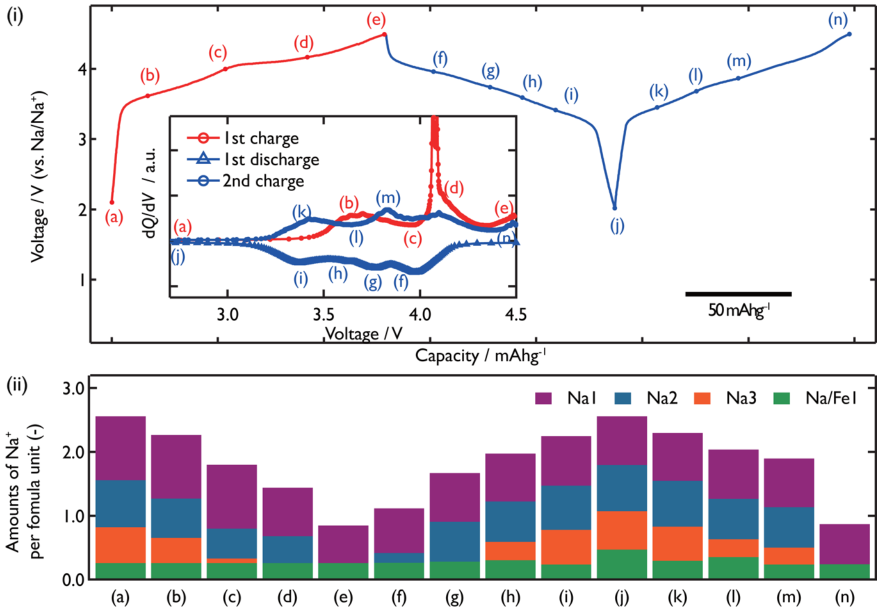

Figure 2. (i) Charge/discharge profiles of $Na_{2.56-y}Fe_{1.72}(SO_4)_3$ at different states of charge (a−n). The initial charge and the following full discharge−charge cycle are shown as red and blue curves, respectively. (Inset) The corresponding dQ/dV profiles, which show an irreversible first charge process and subsequent processes. Note that the features observed on the first discharge and second charge are retained upon further cycling.[22] (ii) Amounts of Na per formula unit in $Na_{2.56-y}Fe_{1.72}(SO_4)_3$ during the electrochemical processes (a−n). Purple, blue, orange, and green bars indicate Na^+ amounts on the Na1, Na2, Na3, and Na/Fe1 sites, respectively.

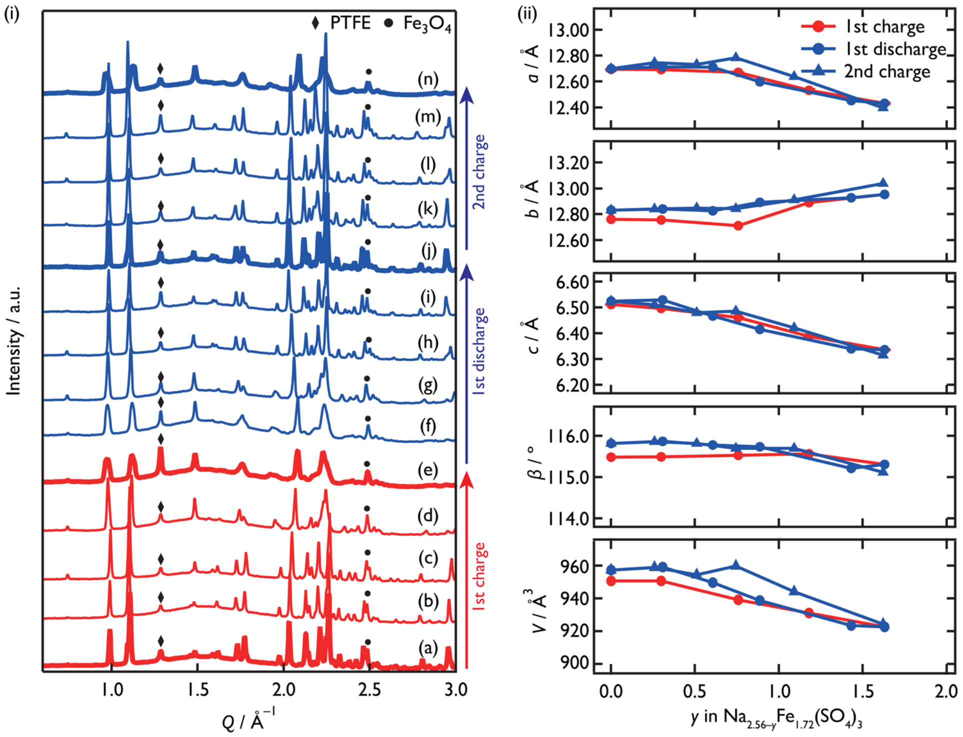

Figure 3. (i) *Ex situ* XRD patterns of $Na_{2.56-y}Fe_{1.72}(SO_4)_3$ at the different states of charge (a−n). The black rhombus and circle mark diffraction peaks of the PTFE binder and Fe_3O_4 impurity phases, respectively. (ii) The variation of lattice parameters a, b, c, and β and the unit cell volume V with monoclinic $C2/c$ symmetry during the first two electrochemical cycles. First charging, discharging, second charging processes are shown in red circles, blue circles, and blue triangles with solid lines, respectively.

change of the nonstoichiometric $Na_{2+2x}Fe_{2-x}(SO_4)_3$ phase (ΔV = ca. 5% for $x = 0.25$) is smaller than that of stoichiometric phase (ΔV = ca. 8% for $x = 0$) based on the full utilization of the Fe^{3+}/Fe^{2+} redox reaction. The detailed calculation results will be reported elsewhere.[56]

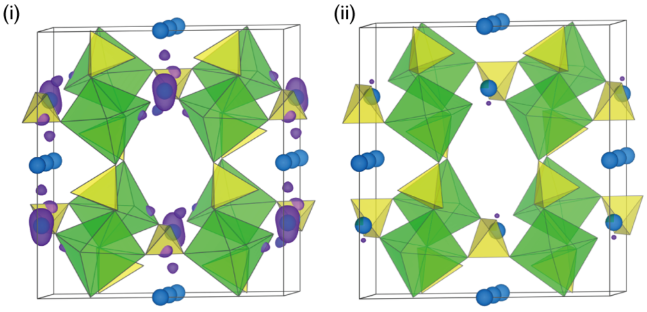

Figure 4. Calculated Fourier difference maps of alluaudite sodium iron sulfate (i) before and (ii) after considering the irreversible Fe migration at stage (d) (cf. Figure 3) upon the charging process. Blue spheres, green octahedra, yellow tetrahedra, and purple isosurfaces (0.1 Å^{-3}) show Na, FeO_6, SO_4, and residual electron density, respectively.

Sodium Intercalation Mechanism. Figure 2(ii) indicates the amount of Na at each crystallographic site during the charge−discharge processes as determined by Rietveld refinements for the *ex situ* XRD patterns. At the initial stage of the charging process (a−c), corresponding to the broad peak observed at 3.67 V in the dQ/dV plot, the occupancy of Na3 site (g_{Na3}) abruptly decreases from 0.561(5) to 0.072(7). This indicates that Na extraction primarily occurred at the Na3 site, which is consistent with the computational results for the shallowest potential of the Na3 site, involving a small migration energy between Na3−Na3 sites (ca. 300 meV).[22,57] At this stage, g_{Na2} decreased by only about 0.27, while g_{Na1} and $g_{Na/Fe1}$ remained constant, where g_{Na2}, g_{Na1}, and $g_{Na/Fe1}$ are the occupancies of Na ions in Na2, Na1 site, and Fe1 site, respectively. On further charging up to (d), after the irreversible sharp peak observed in the dQ/dV plot, a drastic change was observed in the diffraction pattern, which cannot be explained by the occupancy change in mobile Na2 and Na3 sites only.[22,57] The calculated Fourier difference map (Figure 4(i)) indicates positive residual electron density on the Na1 site, suggesting that the site is replaced by heavier ions. Thereby, we adopted a structural model in which Fe migrated into the Na1 site (referred to Fe/Na1 site), as illustrated in Figure 1(ii). For the refinement, the total number of Fe was fixed to unity with linear constraint: $2g_{Fe1} + g_{Fe/Na1} = 1.72$. The refinement based on the proposed model leads to an improvement of the R-factors (e.g., the R-weighted pattern (R_{wp}) reduced from 0.0315 to 0.0285) as well as the disappearance of unreasonable residual electron density on the Na1 site (Figure 4(ii)), where about 16% of Fe at Fe1 site ($\Delta g_{Fe1} = 0.21$) migrated to Na1 site. Using the modified structure formed at time point (d), the bond-valence-sum (BVS) value calculated for Na1 site (expected to be 1.0 for Na^+)[58] increased from 1.06 to 1.49, providing further support for the Fe migration. The mechanism of the migration might be similar to that occurring in $Li_{2-y}FeP_2O_7$ and $Na_{4-y}Fe_3(PO_4)_2(P_2O_7)$,[9] where the driving force is the strong Fe^{3+}−Fe^{3+} Coulombic repulsion within the edge-sharing dimer.[55] In fact, the alluaudite sodium iron sulfate has a shorter Fe−Fe length (3.199 Å) in the edge-sharing Fe_2O_{10} dimer than that in $Li_2FeP_2O_7$ (3.23 Å).

We therefore propose that the sharp peak in the dQ/dV curve at 4.06 V in the first charging process is associated with Na extraction from Na1 site, which then starts to induce Fe^{3+} migration from the Fe1(8f) site into the vacant Na1 (4e) site. At the fully charged state (e), g_{Na2} decreased to 0, and the diffraction peaks were broadened (Figure 3), presumably due to a long-range disordering induced by micro strains, as the peak width showed a reversible change upon subsequent charge/discharge processes. Therefore, throughout the whole initial charging process, Na extraction occurs primarily at Na3 followed by the Na1 and Na2 sites.

In the following discharging process of (e−g), the increase for g_{Na2} dominated, while negligible changes occurred for g_{Na1}, g_{Na3}, and $g_{Na/Fe1}$. Therefore, the cathodic peak at 3.99 V in the dQ/dV plot is attributed to Na insertion into the Na2 site. In the deeper discharge (g−h), g_{Na3} started to increase, showing that the potential peak at 3.76 V is mainly due to Na insertion into the Na3 site. At the last step of the discharging process (h−j), $g_{Na/Fe1}$ increased, while those of the other Na sites remained constant. Thus, the peak at 3.37 V in the dQ/dV plot corresponds to Na insertion into the vacant Fe1 site, which had been occupied by Fe ions before the migration of Fe^{3+} into Na1 site in the first charging process. Throughout the whole discharging process, negligible occupancy change for Fe at Fe1 site (Δg_{Fe1} = ca. 0.09) was observed. Thus, Fe migration occurs in the first charging process but not in the subsequent cycles, which provide reversible features as a battery cathode. Upon the subsequent (second) charging process (j−n), the electrode reaction is reversible tracing the preceding discharging step. Sequential Na extraction occurs in the order of Na/Fe1 followed by Na3 and Na2 sites, pairing the three broad peaks in the dQ/dV plot.

Solid-State NMR Spectroscopy and DFT Calculations. The ^{23}Na MAS NMR spectrum of pristine $Na_{2.56-y}Fe_{1.72}(SO_4)_3$ (y = 0.0) contains a signal centered at 0 ppm with a width of approximately 2500 ppm (Figure 5). NMR experiments performed at different magnetic fields and MAS spinning frequencies show that the additional signals are rotational sidebands (RSB, Figures 5 and S2(i)). An increase of the number of RSBs as well as the significant changes of the NMR line shape signal from low to high magnetic fields (4.7, 7.0, and 16.4 T) at a constant MAS frequency of 60 kHz are in agreement with a linear scaling of the electron−nuclear dipolar coupling with the field strength (Figure 5(i)), suggesting that this interaction dominates.[59] This interaction involves the unpaired electrons of Fe^{2+} in the $t_{2g}^4\ e_g^2$ (high-spin, S = 2) configuration.

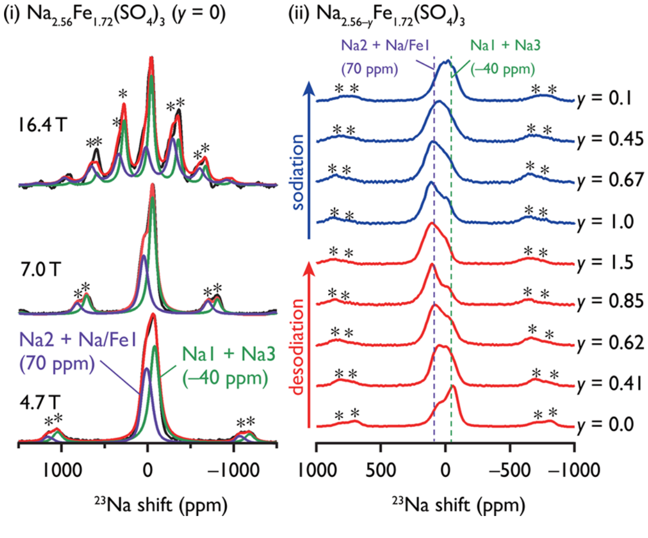

Figure 5. ^{23}Na MAS NMR spectra of $Na_{2.56-y}Fe_{1.72}(SO_4)_3$ at 60 kHz MAS frequency. Rotational sidebands are marked by asterisks. (i) Measurements of pristine $Na_{2.56-y}Fe_{1.72}(SO_4)_3$ (y = 0) in magnetic fields of 4.7, 7.0, and 16.4 T. Experimental data is depicted in black, fitted data in red (significantly overlapped with experimental), and the respective signal contributions of Na2 + Na/Fe1 at 70 ppm in purple as well as Na1 + Na3 at −40 ppm in green (see also Figure S2(i) and Tables S3 and S4). (ii) Measurements of desodiated (red lines) and sodiated (blue) $Na_{2.56-y}Fe_{1.72}(SO_4)_3$ samples at 7.0 T. The assignments of Na2 + Na/Fe1 and Na1 + Na3 based on the pristine material are highlighted by purple and green dotted lines, respectively. The nominal composition is given by the y value on the right side (see also Figure S2(ii)).

Deconvolution and signal line shape fitting results in two ^{23}Na NMR resonances at −40 (green signal) and 70 ppm (purple signal) (Figures 5(i) and S2(i) and Table S3). The hyperfine shifts are relatively small in comparison to shifts seen for oxide materials but not dissimilar to the ^{6,7}Li and ^{23}Na NMR shifts for polyanion-based paramagnetic materials (such as $LiFePO_4$). The smaller shifts are caused by the large inductive effect by the sulfate (or more generally polyanion) groups,[59−62] the covalent S−O bonds creating ionic M−O (M = Na, Fe) bonds, causing a reduced hyperfine (Fermi contact) interaction between the O(2p) and Fe(3d) orbitals, and a respective smaller shift than that usually found for paramagnetic materials.[60] HF-DFT calculations for $Na_{2.50}Fe_{1.75}(SO_4)_3$ result in shift values (Hyb20/Hyb35) of −80/−97, 385/263, 138/65, and 177/91 ppm for Na1, Na2, Na3, and Na/Fe1 (Figure 1(i), Table S4). On the basis of these shift regimes and the hyperfine shift trend of Na1 < Na3 < Na/Fe1 < Na2, the two ^{23}Na NMR signals for pristine $Na_{2.56\text{-}y}Fe_{1.72}(SO_4)_3$ (y = 0.0) are attributed to Na1 + Na3 (green; − 40 ppm) and Na2 + Na/Fe1 (purple; 70 ppm), respectively (Figures 5(i) and S2(i) and Table S3). The sources of the noticeable differences between the calculated and observed hyperfine shifts are ascribed, at least in part, to the neglect of terms such as the pseudocontact shift,[63,64] which are likely to be significant in systems with relatively small Fermi-contact shifts and that contain S = 2, T states (with residual orbital angular momentum; see the Supporting Information for further discussion).

A comparison of the site occupancies derived by Rietveld refinements of the XRD data with the fractions of the two Na environments detected by NMR is 6.2/4.0 (=1.6) vs 0.6/0.4 (=1.5). The calculation is based on Na1(4e) + Na3(4e) and Na2(4b) + Na/Fe1(8f), resulting in $4 \times (1.0 + 0.56)/(4 \times 0.74 + 8 \times 0.13)$ vs the fractions of the ^{23}Na NMR signals for pristine $Na_{2.56}Fe_{1.72}(SO_4)_3$ (Tables S2 and S3). The good agreement of the ratios derived by independent methods supports the analysis of the local atomic environments and their assignments.

The ^{23}Na NMR signals of $Na_{2.56-y}Fe_{1.72}(SO_4)_3$ show significant changes of the line shape and an overall positive shift during desodiation that is reversed during sodiation (Figures 5(ii) and S2(ii)). This is generally due to an increase in the concentration of Fe^{3+} ions with more unpaired electrons in the $t_{2g}^3\ e_g^2$ configuration during desodiation causing stronger electron spin density transfer to the Na and a positive shift and vice versa during the sodiation. Specifically, the decrease in the intensity and shift to more positive frequencies of the negative resonance (assigned to the Na1 and Na3 sites) is assigned, with the aid of the Rietveld refinement results, to the removal of the Na3 Na^+ ions and the oxidation of the Fe^{2+} ions nearby the Na1 sites. Note that the ^{23}Na NMR line shape of the fully sodiated sample (y = 0.1) slightly differs from that of the pristine (y = 0) sample (Figures 5(ii) and S2(ii)). The intensity decrease of the negatively shifted signal is tentatively assigned to the irreversible desodiation from Na1 site at the first charging process, which is consistent with the results of Rietveld refinements.

DOI: 10.1021/acs.chemmater.6b01091
Chem. Mater. 2016, 28, 5321−5328

A more in-depth analysis of the changes in shifts and relative intensities of the different resonances requires a more accurate theoretical description of the ^{23}Na hyperfine shifts. Specifically, DFT-based bond pathway decompositions of hyperfine shifts for environments containing Fe^{2+} and Fe^{3+} ions are needed to unravel underlying spin transfer processes, characterize the atomic environments further, and understand the NMR line shape development during desodiation and sodiation in detail. Additionally, the effects of spin−orbit coupling, such as the pseudo contact shift and zero-field splitting, are neglected here, which will be included in further DFT studies.

Reversible Valence State Changes of Iron (XANES and Mössbauer). To investigate the oxidation state of Fe, we performed *ex situ* XANES measurements during the first charging and discharging processes. As illustrated in Figure 6, the *K*-edge of Fe shifted toward higher energy upon charging with the corresponding features for the pre-edge region (inset of Figure 6), which is consistent with the increase of Fe oxidation state. No isosbestic points were observed, supporting the single-phase reaction mechanism. Upon discharging, both the main- and pre-edges are reversible back toward lower energy. The spectrum at the fully discharged state is very similar to that of the pristine phase, suggesting the Fe^{3+}/Fe^{2+} redox reaction is reversible.

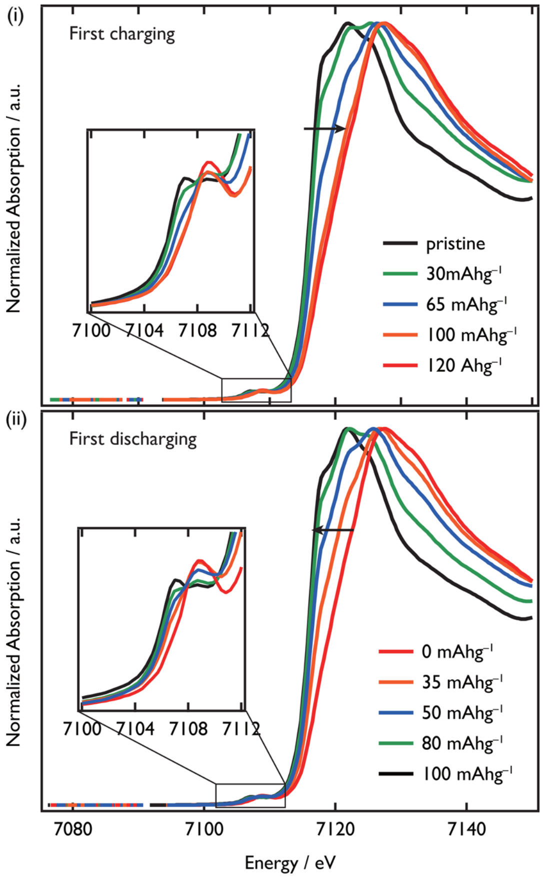

Figure 6. *Ex situ* Fe *K*-edge XANES spectra of $Na_{2.56-y}Fe_{1.72}(SO_4)_3$ at different states of charge. (i) and (ii) indicate spectra acquired upon the initial charging and discharging processes, respectively. The insets are enlargements of the pre-edge regions.

Reversible changes for Fe oxidation states are further confirmed by Mössbauer spectroscopy (Figure S3). The fitting parameters of Mössbauer spectra are shown in Table S5. The line profiles are extensively broadened due to various possible Na arrangements around Fe sites, so distributions of quadrupole splittings (QS) are postulated. A spectrum after the first electrochemical cycle (Figure S3(iii)) shows all of the Fe species are attributed to be Fe^{2+}. These suggest the irreversible capacity ($\sim$16 mAhg^{-1}) is mainly due to the decomposition of the electrolyte and the irreversible Fe migration at the initial charging process gives a minimal effect for reversibility of the Fe^{3+}/Fe^{2+} redox reaction.

■ CONCLUSION

The present study reveals the electrochemical reaction mechanism of alluaudite sodium iron sulfate as a Na-ion battery cathode via a combined approach with diffraction and spectroscopic measurements. The single-phase (solid-solution) reaction occurs involving an irreversible rearrangement reaction upon the first charging process. The origin of the irreversibility is the Na extraction from the Na1 site accompanied by Fe migration from the Fe1 to Na1 site; this mechanism is similar to that of $Li_2FeP_2O_7$ and $Na_4Fe_3(PO_4)_2P_2O_7$. This structural rearrangement is only observed upon the first charging process, and the structural and Fe^{3+}/Fe^{2+} redox reversibility is retained upon the subsequent cycles with a small volume change (ΔV = ca. 3.5%), which contributes to the good cyclability of the electrochemical processes. Sodium extraction occurs primarily at Na3, followed by Na1 and then Na2 sites for the initial charging. The sodium insertion occurred at Na2, Na3, and Na/Fe1 sites for the first discharging and is reversible in subsequent cycles. Understanding of the irreversible reaction and the following reversible reaction mechanism, which might be common among similar crystal structures, should be helpful in the design of new cathode candidates for next generation batteries.

■ ASSOCIATED CONTENT

Ⓢ Supporting Information

The Supporting Information is available free of charge on the ACS Publications website at DOI: 10.1021/acs.chemmater.6b01091.

> Rietveld refinement patterns for *ex situ* synchrotron XRD, ^{23}Na NMR spectra, Mössbauer spectra, refinement parameters for *ex situ* XRD, ^{23}Na NMR, and Mössbauer spectra (PDF)

■ AUTHOR INFORMATION

Corresponding Authors

*E-mail: yamada@chemsys.t.u-tokyo.ac.jp.
*E-mail: cpg27@cam.ac.uk.

Notes

The authors declare no competing financial interest.
Data supporting this work are available from www.repository.cam.ac.uk.

■ ACKNOWLEDGMENTS

Dr. Sai Cheong Chung (The University of Tokyo, Japan), Raphaële J. Clément, Ieuan Seymour, and Dr. Paul M. Bayley (University of Cambridge, UK) are thanked for fruitful discussions. Dr. Prabeer Barpanda is thanked for sharing the magnetic properties data. The present work was financially supported from the Ministry of Education, Culture, Sports, Science and Technology, Japan (MEXT) under the "Element Strategy Initiative for Catalysts & Batteries" (ESICB) project. The synchrotron XRD experiments were performed under KEK-PF User Program (No. 2013G670). Crystal structures and the Fourier difference maps were drawn by VESTA.[65] G.O.

acknowledges financial support from JSPS Research Fellowships under "Materials Education Program for the Future Leaders in Research, Industry, and Technology" (MERIT) project. This project has received funding from the European Union's Horizon 2020 research and innovation program under the Marie Skłodowska-Curie grant agreement No. 655444 (O.P.). R.P. gratefully acknowledges financial support through the Marie Curie Actions People Program of the EU's Seventh Frame work Program (FP7/2007-2013), under the grant agreement n.317127, the 'pNMR project'. K.J.G. gratefully acknowledges funding from The Winston Churchill Foundation of the United States and the Herchel Smith Scholarship. This work made use of the facilities of the Center for Functional Nanomaterials, Brookhaven National Laboratory, which is supported by the U.S. Department of Energy, Office of Basic Energy Sciences, under Contract No. DE-AC02-98CH10886.

■ REFERENCES

(1) Yabuuchi, N.; Yoshida, H.; Komaba, S. Crystal Structures and Electrode Performance of Alpha-$NaFeO_2$ for Rechargeable Sodium Batteries. *Electrochemistry* **2012**, *80*, 716−719.

(2) Kubota, K.; Yabuuchi, N.; Yoshida, H.; Dahbi, M.; Komaba, S. Layered Oxides as Positive Electrode Materials for Na-Ion Batteries. *MRS Bull.* **2014**, *39*, 416−422.

(3) Yabuuchi, N.; Kajiyama, M.; Iwatate, J.; Nishikawa, H.; Hitomi, S.; Okuyama, R.; Usui, R.; Yamada, Y.; Komaba, S. P2-Type $Na_x[Fe_{1/2}Mn_{1/2}]O_2$ Made from Earth-Abundant Elements for Rechargeable Na Batteries. *Nat. Mater.* **2012**, *11*, 512−517.

(4) Moreau, P.; Guyomard, D.; Gaubicher, J.; Boucher, F. Structure and Stability of Sodium Intercalated Phases in Olivine $NaFePO_4$. *Chem. Mater.* **2010**, *22*, 4126−4128.

(5) Lu, J.; Chung, S. C.; Nishimura, S.; Yamada, A. Phase Diagram of Olivine Na_xFePO_4. *Chem. Mater.* **2013**, *25*, 4557−4565.

(6) Ellis, B. L.; Makahnouk, W. R. M.; Makimura, Y.; Toghill, K.; Nazar, L. F. A Multifunctional 3.5 V Iron-Based Phosphate Cathode for Rechargeable Batteries. *Nat. Mater.* **2007**, *6*, 749−753.

(7) Barpanda, P.; Liu, G.; Ling, C. D.; Tamaru, M.; Avdeev, M.; Chung, S.-C.; Yamada, Y.; Yamada, A. $Na_2FeP_2O_7$: A Safe Cathode for Rechargeable Sodium-Ion Batteries. *Chem. Mater.* **2013**, *25*, 3480−3487.

(8) Kim, H.; Park, I.; Seo, D.-H.; Lee, S.; Kim, S.-W.; Kwon, W. J.; Park, Y.-U.; Kim, C. S.; Jeon, S.; Kang, K. New Iron-Based Mixed-Polyanion Cathodes for Lithium and Sodium Rechargeable Batteries: Combined First Principles Calculations and Experimental Study. *J. Am. Chem. Soc.* **2012**, *134*, 10369−10372.

(9) Kim, H.; Park, I.; Lee, S.; Kim, H.; Park, K.-Y.; Park, Y.-U.; Kim, H.; Kim, J.; Lim, H.-D.; Yoon, W.-S.; Kang, K. Understanding the Electrochemical Mechanism of the New Iron-Based Mixed-Phosphate $Na_4Fe_3(PO_4)_2(P_2O_7)$ in a Na Rechargeable Battery. *Chem. Mater.* **2013**, *25*, 3614−3622.

(10) Padhi, A. K. Tuning the Position of the Redox Couples in Materials with NASICON Structure by Anionic Substitution. *J. Electrochem. Soc.* **1998**, *145*, 1518.

(11) Recham, N.; Chotard, J.-N.; Dupont, L.; Delacourt, C.; Walker, W.; Armand, M.; Tarascon, J.-M. A 3.6 V Lithium-Based Fluorosulphate Insertion Positive Electrode for Lithium-Ion Batteries. *Nat. Mater.* **2010**, *9*, 68−74.

(12) Barpanda, P.; Ati, M.; Melot, B. C.; Rousse, G.; Chotard, J.-N.; Doublet, M.-L.; Sougrati, M. T.; Corr, S. A.; Jumas, J.-C.; Tarascon, J.-M. A 3.90 V Iron-Based Fluorosulphate Material for Lithium-Ion Batteries Crystallizing in the Triplite Structure. *Nat. Mater.* **2011**, *10*, 772−779.

(13) Recham, N.; Rousse, G.; Sougrati, M. T.; Chotard, J.-N.; Frayret, C.; Mariyappan, S.; Melot, B. C.; Jumas, J.-C.; Tarascon, J.-M. Preparation and Characterization of a Stable $FeSO_4F$ Based Framework for Alkali Ion Insertion Electrodes. *Chem. Mater.* **2012**, *24*, 4363−4370.

(14) Subban, C. V.; Ati, M.; Rousse, G.; Abakumov, A. M.; Van Tendeloo, G.; Janot, R.; Tarascon, J.-M. Preparation, Structure, and Electrochemistry of Layered Polyanionic Hydroxysulfates: $LiMSO_4OH$ (M = Fe, Co, Mn) Electrodes for Li-Ion Batteries. *J. Am. Chem. Soc.* **2013**, *135*, 3653−3661.

(15) Reynaud, M.; Ati, M.; Melot, B. C.; Sougrati, M. T.; Rousse, G.; Chotard, J.-N.; Tarascon, J.-M. $Li_2Fe(SO_4)_2$ as a 3.83V Positive Electrode Material. *Electrochem. Commun.* **2012**, *21*, 77−80.

(16) Lander, L.; Reynaud, M.; Rousse, G.; Sougrati, M. T.; Laberty-Robert, C.; Messinger, R. J.; Deschamps, M.; Tarascon, J.-M. Synthesis and Electrochemical Performance of the Orthorhombic $Li_2Fe(SO_4)_2$ Polymorph for Li-Ion Batteries. *Chem. Mater.* **2014**, *26*, 4178−4189.

(17) Sun, M.; Rousse, G.; Abakumov, A. M.; Van Tendeloo, G.; Sougrati, M.-T.; Courty, M.; Doublet, M.-L.; Tarascon, J.-M. An Oxysulfate $Fe_2O(SO_4)_2$ Electrode for Sustainable Li-Based Batteries. *J. Am. Chem. Soc.* **2014**, *136*, 12658−12666.

(18) Reynaud, M.; Rousse, G.; Abakumov, A. M.; Sougrati, M. T.; Van Tendeloo, G.; Chotard, J.-N.; Tarascon, J.-M. Design of New Electrode Materials for Li-Ion and Na-Ion Batteries from the Bloedite Mineral $Na_2Mg(SO_4)_2{\cdot}4H_2O$. *J. Mater. Chem. A* **2014**, *2*, 2671−2680.

(19) Barpanda, P.; Oyama, G.; Ling, C. D.; Yamada, A. Kröhnkite-Type $Na_2Fe(SO_4)_2{\cdot}2H_2O$ as a Novel 3.25 V Insertion Compound for Na-Ion Batteries. *Chem. Mater.* **2014**, *26*, 1297−1299.

(20) Barpanda, P.; Chotard, J.-N.; Recham, N.; Delacourt, C.; Ati, M.; Dupont, L.; Armand, M.; Tarascon, J.-M. Structural, Transport, and Electrochemical Investigation of Novel $AMSO_4F$ (A = Na, Li; M = Fe, Co, Ni, Mn) Metal Fluorosulphates Prepared Using Low Temperature Synthesis Routes. *Inorg. Chem.* **2010**, *49*, 7401−7413.

(21) Ati, M.; Dupont, L.; Recham, N.; Chotard, J.-N. J. N.; Walker, W. T.; Davoisne, C.; Barpanda, P.; Sarou-Kanian, V.; Armand, M.; Tarascon, J.-M. J. M. Synthesis, Structural, and Transport Properties of Novel Bihydrated Fluorosulphates $NaMSO_4F{\cdot}2H_2O$ (M = Fe, Co, and Ni). *Chem. Mater.* **2010**, *22*, 4062−4068.

(22) Barpanda, P.; Oyama, G.; Nishimura, S.; Chung, S. C.; Yamada, A. A 3.8-V Earth-Abundant Sodium Battery Electrode. *Nat. Commun.* **2014**, *5*, 4358.

(23) Fisher, D. J. Alluaudite. *Am. Mineral.* **1955**, *40*, 1100−1109.

(24) Oyama, G.; Nishimura, S.; Suzuki, Y.; Okubo, M.; Yamada, A. Off-Stoichiometry in Alluaudite-Type Sodium Iron Sulfate $Na_{2+2x}Fe_{2-x}(SO_4)_3$ as an Advanced Sodium Battery Cathode Material. *ChemElectroChem* **2015**, *2*, 1019−1023.

(25) Chung, S. C.; Barpanda, P.; Nishimura, S.; Yamada, Y.; Yamada, A. Polymorphs of $LiFeSO_4F$ as Cathode Materials for Lithium Ion Batteries − a First Principle Computational Study. *Phys. Chem. Chem. Phys.* **2012**, *14*, 8678.

(26) Komaba, S.; Ishikawa, T.; Yabuuchi, N.; Murata, W.; Ito, A.; Ohsawa, Y. Fluorinated Ethylene Carbonate as Electrolyte Additive for Rechargeable Na Batteries. *ACS Appl. Mater. Interfaces* **2011**, 3, 4165−4168.

(27) Harris, R. K.; Becker, E. D.; Cabral de Menezes, S. M.; Goodfellow, R.; Granger, P. NMR Nomenclature: Nuclear Spin Properties and Conventions for Chemical Shifts. IUPAC Recommendations 2001. International Union of Pure and Applied Chemistry. Physical Chemistry Division. Commission on Molecular Structure and Spectroscopy. *Magn. Reson. Chem.* **2002**, *40*, 489−505.

(28) Massiot, D.; Fayon, F.; Capron, M.; King, I.; Le Calve, S.; Alonso, B.; Durand, J.-O.; Bujoli, B.; Gan, Z.; Hoatson, G. Modelling One- and Two-Dimensional Solid-State NMR Spectra. *Magn. Reson. Chem.* **2002**, *40*, 70−76.

(29) Ravel, B.; Newville, M. ATHENA, ARTEMIS, HEPHAESTUS: Data Analysis for X-Ray Absorption Spectroscopy Using IFEFFIT. *J. Synchrotron Radiat.* **2005**, *12*, 537−541.

(30) Kresse, G.; Hafner, J. Ab Initio Molecular Dynamics for Liquid Metals. *Phys. Rev. B: Condens. Matter Mater. Phys.* **1993**, *47*, 558−561.

(31) Kresse, G.; Hafner, J. Ab Initio Molecular-Dynamics Simulation of the Liquid-Metal−amorphous-Semiconductor Transition in Germanium. *Phys. Rev. B: Condens. Matter Mater. Phys.* **1994**, *49*, 14251−14269.

(32) Kresse, G.; Furthmüller, J. Efficiency of Ab-Initio Total Energy Calculations for Metals and Semiconductors Using a Plane-Wave Basis Set. *Comput. Mater. Sci.* **1996**, *6*, 15−50.

(33) Hohenberg, P.; Kohn, W. Inhomogeneous Electron Gas. *Phys. Rev.* **1964**, *136*, B864−B871.

(34) Kohn, W.; Sham, L. J. Self-Consistent Equations Including Exchange and Correlation Effects. *Phys. Rev.* **1965**, *140*, A1133−A1138.

(35) Blöchl, P. E. Projector Augmented-Wave Method. *Phys. Rev. B: Condens. Matter Mater. Phys.* **1994**, *50*, 17953−17979.

(36) Kresse, G.; Joubert, D. From Ultrasoft Pseudopotentials to the Projector Augmented-Wave Method. *Phys. Rev. B: Condens. Matter Mater. Phys.* **1999**, *59*, 1758−1775.

(37) Perdew, J. P.; Burke, K.; Ernzerhof, M. Generalized Gradient Approximation Made Simple. *Phys. Rev. Lett.* **1996**, *77*, 3865−3868.

(38) Perdew, J. P.; Burke, K.; Ernzerhof, M. Generalized Gradient Approximation Made Simple [Phys. Rev. Lett. 77, 3865 (1996)]. *Phys. Rev. Lett.* **1997**, *78*, 1396−1396.

(39) Anisimov, V. I.; Zaanen, J.; Andersen, O. K. Band Theory and Mott Insulators: Hubbard U instead of Stoner I. *Phys. Rev. B: Condens. Matter Mater. Phys.* **1991**, *44*, 943−954.

(40) Anisimov, V. I.; Solovyev, I. V.; Korotin, M. A.; Czyżyk, M. T.; Sawatzky, G. A. Density-Functional Theory and NiO Photoemission Spectra. *Phys. Rev. B: Condens. Matter Mater. Phys.* **1993**, *48*, 16929−16934.

(41) Liechtenstein, A. I.; Anisimov, V. I.; Zaanen, J. Density-Functional Theory and Strong Interactions: Orbital Ordering in Mott-Hubbard Insulators. *Phys. Rev. B: Condens. Matter Mater. Phys.* **1995**, *52*, R5467−R5470.

(42) Zhou, F.; Cococcioni, M.; Kang, K.; Ceder, G. The Li Intercalation Potential of $\mathrm{Li}M\mathrm{PO}_4$ and $\mathrm{Li}M\mathrm{SiO}_4$ Olivines with M = Fe, Mn, Co, Ni. *Electrochem. Commun.* **2004**, *6*, 1144−1148.

(43) Zhou, F.; Kang, K.; Maxisch, T.; Ceder, G.; Morgan, D. The Electronic Structure and Band Gap of $LiFePO_4$ and $LiMnPO_4$. *Solid State Commun.* **2004**, *132*, 181−186.

(44) Dovesi, R.; Orlando, R.; Civalleri, B.; Roetti, C.; Saunders, V. R.; Zicovich-Wilson, C. M. CRYSTAL: A Computational Tool for the Ab Initio Study of the Electronic Properties of Crystals. *Z. Kristallogr. - Cryst. Mater.* **2005**, *220*, 571−573.

(45) Muscat, J.; Wander, A.; Harrison, N. M. On the Prediction of Band Gaps from Hybrid Functional Theory. *Chem. Phys. Lett.* **2001**, *342*, 397−401.

(46) Cora, F.; Alfredsson, M.; Mallia, G.; Middlemiss, D. S.; Mackrodt, W. C.; Dovesi, R.; Orlando, R. *Principles and Applications of Density Functional Theory in Inorganic Chemistry II*, 1st ed.; Kaltsoyannis, N., McGrady, J. E., Eds.; Springer: Berlin, Germany, 2004.

(47) Feng, X.; Harrison, N. M. Magnetic Coupling Constants from a Hybrid Density Functional with 35% Hartree-Fock Exchange. *Phys. Rev. B: Condens. Matter Mater. Phys.* **2004**, *70*, 092402.

(48) Middlemiss, D. S.; Lawton, L. M.; Wilson, C. C. A Solid-State Hybrid Density Functional Theory Study of Prussian Blue Analogues and Related Chlorides at Pressure. *J. Phys.: Condens. Matter* **2008**, *20*, 335231.

(49) de P. R. Moreira, I.; Illas, F.; Martin, R. L. Effect of Fock Exchange on the Electronic Structure and Magnetic Coupling in NiO. *Phys. Rev. B: Condens. Matter Mater. Phys.* **2002**, *65*, 155102.

(50) Kim, J.; Middlemiss, D. S.; Chernova, N. A.; Zhu, B. Y. X.; Masquelier, C.; Grey, C. P. Linking Local Environments and Hyperfine Shifts: A Combined Experimental and Theoretical (31)P and (7)Li Solid-State NMR Study of Paramagnetic Fe(III) Phosphates. *J. Am. Chem. Soc.* **2010**, *132*, 16825−16840.

(51) Dwibedi, D.; Barpanda, P. Alluaudite Family of Sodium Insertion Compounds: Scalable Synthesis, Polymorphorphism and Electrochemistry. In *Battery Meeting*; 2015; p 111.

(52) Nytén, A.; Abouimrane, A.; Armand, M.; Gustafsson, T.; Thomas, J. O. Electrochemical Performance of Li_2FeSiO_4 as a New Li-Battery Cathode Material. *Electrochem. Commun.* **2005**, *7*, 156−160.

(53) Masese, T.; Orikasa, Y.; Tassel, C.; Kim, J.; Minato, T.; Arai, H.; Mori, T.; Yamamoto, K.; Kobayashi, Y.; Kageyama, H.; Ogumi, Z.; Uchimoto, Y. Relationship between Phase Transition Involving Cationic Exchange and Charge−Discharge Rate in Li_2FeSiO_4. *Chem. Mater.* **2014**, *26*, 1380−1384.

(54) Shimizu, D.; Nishimura, S.; Barpanda, P.; Yamada, A. Electrochemical Redox Mechanism in 3.5 V Li_{2-x} FeP_2O_7 ($0 \leq x \leq 1$) Pyrophosphate Cathode. *Chem. Mater.* **2012**, *24*, 2598−2603.

(55) Ye, T.; Barpanda, P.; Nishimura, S.; Furuta, N.; Chung, S.-C.; Yamada, A. General Observation of Fe^{3+}/Fe^{2+} Redox Couple Close to 4 V in Partially Substituted $Li_2FeP_2O_7$ Pyrophosphate Solid-Solution Cathodes. *Chem. Mater.* **2013**, *25*, 3623−3629.

(56) Chung, S. C.; Oyama, G.; Yamada, A., in preparation.

(57) Wong, L. L.; Chen, H. M.; Adams, S. Sodium-Ion Diffusion Mechanisms in the Low Cost High Voltage Cathode Material $Na_{(2+\delta)}Fe_{(2-\delta/2)}(SO_4)_3$. *Phys. Chem. Chem. Phys.* **2015**, *17*, 9186−9193.

(58) Brown, I. D. Recent Developments in the Methods and Applications of the Bond Valence Model. *Chem. Rev.* **2009**, *109*, 6858−6919.

(59) Grey, C. P.; Dupré, N. NMR Studies of Cathode Materials for Lithium-Ion Rechargeable Batteries. *Chem. Rev.* **2004**, *104*, 4493−4512.

(60) Clément, R. J.; Bruce, P. G.; Grey, C. P. Review—Manganese-Based P2-Type Transition Metal Oxides as Sodium-Ion Battery Cathode Materials. *J. Electrochem. Soc.* **2015**, *162*, A2589−A2604.

(61) Clément, R. J.; Pell, A. J.; Middlemiss, D. S.; Strobridge, F. C.; Miller, J. K.; Whittingham, M. S.; Emsley, L.; Grey, C. P.; Pintacuda, G. Spin-Transfer Pathways in Paramagnetic Lithium Transition-Metal Phosphates from Combined Broadband Isotropic Solid-State MAS NMR Spectroscopy and DFT Calculations. *J. Am. Chem. Soc.* **2012**, *134*, 17178−17185.

(62) Middlemiss, D. S.; Ilott, A. J.; Clément, R. J.; Strobridge, F. C.; Grey, C. P. Density Functional Theory-Based Bond Pathway Decompositions of Hyperfine Shifts: Equipping Solid-State NMR to Characterize Atomic Environments in Paramagnetic Materials. *Chem. Mater.* **2013**, *25*, 1723−1734.

(63) Vaara, J. Theory and Computation of Nuclear Magnetic Resonance Parameters. *Phys. Chem. Chem. Phys.* **2007**, *9*, 5399−5418.

(64) Bertini, I.; Luchinat, C.; Parigi, G. Magnetic Susceptibility in Paramagnetic NMR. *Prog. Nucl. Magn. Reson. Spectrosc.* **2002**, *40*, 249−273.

(65) Momma, K.; Izumi, F. VESTA 3 for Three-Dimensional Visualization of Crystal, Volumetric and Morphology Data. *J. Appl. Crystallogr.* **2011**, *44*, 1272−1276.